Heterostructure Manipulation via in Situ Localized Phase Transformation for High-Rate and Highly Durable Lithium Ion Storage

Junnan Hao
University of Wollongong, jh845@uowmail.edu.au

Jian Zhang
Changsha University of Science And Technology

Guanglin Xia
University of Wollongong, guanglin@uow.edu.au

Yajie Liu
University of Wollongong, yl327@uowmail.edu.au

Yang Zheng
University of Wollongong, yz966@uowmail.edu.au

See next page for additional authors

Recommended Citation

Heterostructure Manipulation via in Situ Localized Phase Transformation for High-Rate and Highly Durable Lithium Ion Storage

Abstract

Recently, heterostructures have attracted much attention in widespread research fields. By tailoring the physicochemical properties of the two components, creating heterostructures endows composites with diverse functions due to the synergistic effects and interfacial interaction. Here, a simple in situ localized phase transformation method is proposed to transform the transition-metal oxide electrode materials into heterostructures. Taking molybdenum oxide as an example, quasi-core-shell $MoO_3@MoO_2$ heterostructures were successfully fabricated, which were uniformly anchored on reduced graphene oxide (rGO) for high-rate and highly durable lithium ion storage. The in situ introduction of the MoO_2 shell not only effectively enhances the electronic conductivity but also creates $MoO_3@MoO_2$ heterojunctions with abundant oxygen vacancies, which induces an inbuilt driving force at the interface, enhancing ion/electron transfer. In operando synchrotron X-ray powder diffraction has confirmed the excellent phase reversibility of the MoO_2 shell during charge/discharge cycling, which contributes to the excellent cycling stability of the $MoO_3@MoO_2$/rGO electrode (1208.9 mAh g-1 remaining at 5 A g-1 after 2000 cycles). This simple in situ heterostructure fabrication method provides a facile way to optimize electrode materials for high-performance lithium ion batteries and possibly other energy storage devices.

Disciplines

Engineering | Physical Sciences and Mathematics

Publication Details

Authors

Junnan Hao, Jian Zhang, Guanglin Xia, Yajie Liu, Yang Zheng, Wenchao Zhang, Yongbing Tang, Wei Kong Pang, and Zaiping Guo

Heterostructure Manipulation *via In-Situ* Localized Phase Transformation for High-Rate and Highly Durable Lithium Ion Storage

Junnan Hao[†], Jian Zhang[‡], Guanglin Xia[†], Yajie Liu[†], Yang Zheng[†], Wenchao Zhang[†], Yongbing Tang[*][§], Wei Kong Pang[†], Zaiping Guo*[†]

[†] Institute for Superconducting & Electronic Materials, School of Mechanical, Materials and Mechatronics Engineering, University of Wollongong, Wollongong, NSW 2522, Australia

[‡] College of Automotive and Mechanical Engineering, Changsha University of Science and Technology, Changsha 410114, China

[§] Functional Thin Films Research Center; Shenzhen Institutes of Advanced Technology, Chinese Academy of Sciences, Shenzhen 518055, China

Corresponding Author: [*] tangyb@siat.ac.cn; zguo@uow.edu.au

ABSTRACT：

Recently, heterostructures have attracted much attention in widespread research fields. By tailoring the physicochemical properties of the two components, creating heterostructures endows composites with diverse functions due to the synergistic effects and interfacial interaction. Here, a simple *in-situ* localized phase transformation method is proposed to transform the transition metal oxide electrode materials into heterostructures. Taking molybdenum oxide as an example, quasi-core-shell $MoO_3@MoO_2$ heterostructures were successfully fabricated, which were uniformly anchored on reduced graphene oxide (rGO) for high-rate and highly durable lithium ion storage. The *in-situ* introduction of the MoO_2 shell not only effectively enhances the electronic conductivity, but also creates $MoO_3@MoO_2$ heterojunctions with abundant oxygen vacancies, which induces an inbuilt driving force at the interface, enhancing ion/electron transfer. In-operando synchrotron X-ray powder

diffraction has confirmed the excellent phase reversibility of the MoO_2 shell during charge/discharge cycling, which contributes to the excellent cycling stability of the $MoO_3@MoO_2$/rGO electrode (1208.9 mAh g^{-1} remaining at 5 A g^{-1} after 2000 cycles). This simple *in-situ* heterostructure fabrication method provides a facile way to optimize electrode materials for high-performance lithium ion batteries and possibly other energy storage devices.

Heterostructures can be formed by modulating different compositions and/or doping to enable passivation of interfaces, where the electronic band structure near the interface will be changed according to the electrostatics.[1] Because of their interface effects, heterostructures with distinct functionality often exhibit enhanced performance in many electronic devices, including solar cells, ultrathin photodetectors, semiconductor lasers, and tunneling transistors.[2-4] It has been claimed that building heterostructures though coupling components with different electronic energy band gaps will improve the surface reaction kinetics and facilitate charge transport due to the benefit of the internal electric field at the interface. For instance, fast ion conduction has been demonstrated in nanometer-scale CaF_2/BaF_2 heterostructures.[5] Benefiting from the synergistic effects, two-dimensional (2D)-mesoporous-carbon/MoS_2 heterostructures exhibited outstanding cycling stability and high-rate performance in lithium ion batteries (LIBs).[6] Due to integration of the merits of the different components and reversible electron/ion transport at the interface, SnO_2/MXene and TiO_2/MXene heterostructures showed high capacity and extraordinary high-rate performance for Li ion storage.[7] Inspired by previous research, we believe that transition metal oxide heterostructures can be manipulated *via in-situ* localized phase transformation as electrode materials with excellent performance in energy storage devices.

Owing to its high theoretical capacity (1117.3 mAh g^{-1}), α-MoO_3 with a bilayer structure has attracted much attention as an attractive candidate anode for LIBs.[8] The Li storage performance of MoO_3 is severely restricted, however, by its sluggish Li ion diffusion kinetics.[9] A variety of strategies have been claimed to enhance the kinetic of MoO_3.[10] Nanostructuring is one of the most widespread strategies, and various nanostructured forms of MoO_3, including nanowires, nanorods, and nanosheets, have been reported to boost the Li storage kinetics.[11] Unfortunately, self-aggregation and the volume expansion of nanomaterials severely limit the beneficial effects of nanostructuring.[12] Introducing a conductive matrix into

MoO$_3$ is another common strategy to enhance the electronic conductivity of MoO$_3$.[13] The main drawback of this strategy, however, is that only near-surface materials, which have intimate contact with the conductive matrix, could experience enhanced electronic conductivity.[14] Consequently, achieving MoO$_3$-based materials with excellent high-rate performance and cycling stability still remains a huge challenge.[15-19]

Monoclinic MoO$_2$, although having lower capacity (837.6 mAh g^{-1}) compared with α-MoO$_3$, is also an anode candidate for LIBs, resulting from its metallic electrical conductivity and facile ion transport properties.[13, 20] Based on the solid-state reaction kinetics, the transformation from α-MoO$_3$ to MoO$_2$ preferentially occurs in a perpendicular direction to the crystalline layers of α-MoO$_3$ during thermal reduction ([010] direction), and thus, it is believed that α-MoO$_3$/MoO$_2$ heterojunctions could be created, which could be an effective way to achieve molybdenum oxide electrodes with high electrical conductivity and good structural stability, as well as high capacity.[21-22] In addition, oxygen vacancies formed at the heterointerface could create atomic defects, structural distortion, and an unbalanced charge distribution at the interface, which would provide an inbuilt charge-transfer driving force,[23-24] facilitating interfacial electron transport and accelerating the Li$^+$ ion diffusion kinetics in the electrode.[15]

Herein, a facile localized phase transformation strategy was adopted for *in-situ* fabrication of MoO$_2$ coated α-MoO$_3$ heterostructures, which were homogeneously decorated on reduced graphene oxide (MoO$_3$@MoO$_2$/rGO) sheets. The homogeneous coating of MoO$_2$ and the uniform distribution of MoO$_3$@MoO$_2$ heterostructures on rGO could effectively improve the electrical conductivity. The oxygen vacancies generated at the interface of MoO$_3$ and MoO$_2$ with the reduction of MoO$_3$ create desirable interfacial effects, which was further confirmed by density functional theory (DFT) calculations. In-operando synchrotron X-ray powder diffraction (XRPD) further verified the high reversibility of the MoO$_2$ shell during cycling,

4

which helps to enhance the cycling stability. Thanks to these structural advantages, the MoO$_3$@MoO$_2$/rGO-500 electrode delivered a high capacity of 1340.0 mAh g^{-1} at 100 mA g^{-1} and outstanding cycling stability, with a capacity of 1208.9 mAh g^{-1} remaining after 2000 cycles at 5 A g^{-1}. This work demonstrates an effective way to enhance the Li storage kinetics *via* the construction of interfaces and the introduction of heterostructures by *in-situ* oxidation/reduction. The proposed heterostructure manipulation strategy could also be extended to other transition metal oxide electrodes for energy storage and conversion.

RESULTS AND DISCUSSION

One-step *in-situ* phase transformation was employed to prepare MoO$_3$@MoO$_2$/rGO with (NH$_4$)$_6$Mo$_7$O$_{24}$ chosen as the Mo source. To investigate the phase transformation of (NH$_4$)$_6$Mo$_7$O$_{24}$/graphene oxide (GO) during the calcining process, thermogravimetric analysis (TGA) was conducted in argon (Figure 1a) and air flow (Figure S1 in the Supporting Information), respectively. Four weight loss regions can be observed in Figure 1a: the weight losses in the temperature range of 50–180 °C and 180–300 °C originate from the removal of interlayer moisture and the decomposition of (NH$_4$)$_6$Mo$_7$O$_{24}$, respectively.[25] The following stage from 300 to 420 °C corresponds to the removal of oxygen-containing functional groups from the GO sheets. Subsequently, α-MoO$_3$ is gradually reduced into MoO$_2$ from 420 °C and completely converted into MoO$_2$ when the temperature reaches 550 °C. This result validates the possibility of fabricating MoO$_3$@MoO$_2$ heterojunctions through controlling the heat-treatment temperature, as evidenced by the X-ray diffraction (XRD) results (Figure 1b). The product synthesized at 400 °C (denoted as MoO$_3$/rGO-400) has only characteristic peaks corresponding to MoO$_3$.[26] While characteristic peaks assigned to monoclinic MoO$_2$ appear with weakening of the peak intensity of α-MoO$_3$ simultaneously after thermal annealing of the samples at 450 and 500 °C (MoO$_3$@MoO$_2$/rGO-450 and MoO$_3$@MoO$_2$/rGO-500, respectively), indicating both samples contain the MoO$_3$ and MoO$_2$ phase. On further

increasing the heating temperature to 600 °C, only MoO_2 peaks can be observed with the complete disappearance of peaks for MoO_3 (MoO_2/rGO-600).[20]

X-ray photoelectron spectroscopy (XPS) measurements were further adopted to characterize the oxidation state of molybdenum in different samples (Figure S2 and Figure 1c). The Mo 3d spectrum of MoO_3/rGO-400 (Figure S2a) is mainly occupied by Mo^{6+} with a spin-orbit doublet peaks at binding energies of 232.3 ± 0.1 and 236.0 ± 0.1 eV.[27-28] After heating to 600 °C, $3d^{4+}_{3/2}$ and $3d^{4+}_{5/2}$ peaks belonging to MoO_2 could be observed (Figure S2b).[29] By comparison, the Mo 3d spectrum of MoO_3@MoO_2/rGO-500 reveals the simultaneous presence of characteristic peaks belonging to Mo^{4+} and Mo^{6+}, and the peak intensity of Mo^{6+} is increased after etching the surface with argon plasma to remove the surface layer (Figure 1c).[15] Further calculations demonstrated that the content of Mo^{6+} increased from 33.4% to 39.8% after argon plasma etching (Table S1), which indicates that the majority of the MoO_3 was reduced to MoO_2, with the MoO_3 occupying the inner part of the heterostructure, while the MoO_2 is mainly located in the outer part (schematic illustration shown in Figure S3).

The morphology of MoO_3@MoO_2/rGO and the phase transfer process to form the MoO_3@MoO_2 heterostructure in MoO_3@MoO_2/rGO-500 were further investigated by scanning electron microscopy (SEM) and transmission electron microscopy (TEM). It is obvious that the small nanosheets of MoO_3@MoO_2 are uniformly anchored on the rGO sheets, as shown in Figure 1d. The MoO_3@MoO_2 heterostructured particles, however, suffer from serious aggregation without rGO support (Figure S4). The TEM results further verified the homogeneous dispersion of lamellar MoO_3@MoO_2 heterostructures with widths of ~200 nm (Figure 1e). Atomic force microscopy (Figure 1f) confirmed that the thickness of the MoO_3@MoO_2 nanosheets is ~5 nm. These MoO_3@MoO_2 nanosheets guarantee facile strain relaxation and help to alleviate the volume expansion of the MoO_3 inside.[30] In comparison, MoO_3@rGO-400 and MoO_2/rGO-600 show similar morphology (Figures S5a

and S6a). The high-resolution TEM (HRTEM) image of MoO$_3$@rGO-400 (Figure S5c) shows lattice spacing of 0.326 nm, which can be assigned to the (021) crystal planes of α-MoO$_3$. This agrees well with the selected area electron diffraction (SAED) pattern (Figure S5b). In the HRTEM image of MoO$_2$/rGO-600, a uniform lattice spacing of 0.342 nm, which corresponds to the (011) planes of monoclinic MoO$_2$, can be observed (Figure S6c). For the MoO$_3$@MoO$_2$/rGO-500 sample, however, the corresponding SAED pattern (Figure 1k) confirms the polycrystalline nature of MoO$_3$@MoO$_2$ heterojunctions, including both MoO$_2$ and MoO$_3$ phases. Furthermore, a lattice spacing of 0.342 nm, characteristic of the (011) planes of MoO$_2$, can be observed on the boundary and it crosses the whole surface (Figure 1l), whereas the internal lattice spacing (0.326 nm) corresponds to the (021) planes of α-MoO$_3$, revealing that MoO$_2$ is generated on the border and at the surface of MoO$_3$ *via in-situ* localized phase transformation, which is consistent with the reduction mechanism of α-MoO$_3$.[31] The localized phase transformation and formation of MoO$_2$ at the edge and surface could shorten the electron/ion transfer pathways in the inner MoO$_3$, thus not only enhancing the electrical conductivity, but also creating MoO$_3$@MoO$_2$ heterostructures, which can tailor the physicochemical characteristics of the two building blocks and endow MoO$_3$@MoO$_2$ with excellent performance due to the synergistic effects.[32] More interestingly, according to the reduction mechanism of α-MoO$_3$, lattice oxygen O$_{(3)}$ on the (010) facet was reduced, resulting in oxygen vacancies at the interface of MoO$_3$ and MoO$_2$, as verified by electron paramagnetic resonance (EPR) (Figure S7).[33] The oxygen vacancies at the interface cause an unbalanced charge distribution, which helps to promote interfacial charge transfer.[34-35]

To compare the Li storage performance of MoO$_3$, MoO$_2$, and MoO$_3$@MoO$_2$ heterostructures, MoO$_3$/rGO, MoO$_3$@MoO$_2$/rGO, and MoO$_2$/rGO electrodes were investigated using discharge−charge cycling and cyclic voltammograms (CVs) in coin cells. Figure 2a and Figures S8, 9 show the typical discharge−charge curves of the different electrodes at 100 mA

g^{-1}. In the case of MoO$_3$/rGO-400 electrode, only an obvious discharge platform below 0.4 V can be observed, which is consistent with its CV curves (Figure S10a). The discharge capacity of MoO$_3$/rGO-400 is 853.1 mAh g^{-1}, still much lower than the theoretical specific capacity of α-MoO$_3$. The MoO$_3$@MoO$_2$/rGO-500 and MoO$_2$/rGO-600 electrodes exhibit three discharge plateaus between 1.0 V and 2.0 V, indicating the phase transitions of MoO$_2$ in the Li insertion process from the original monoclinic to the orthorhombic phase and then from the orthorhombic to the monoclinic phase.[36] The discharge capacity of the MoO$_3$@MoO$_2$/rGO-500 heterostructure is ~1340.0 mAh g^{-1}, much higher than those for the bare MoO$_3$/rGO-400 and MoO$_2$/rGO-600 electrodes, and the MoO$_3$@MoO$_2$-500 without rGO. Figure 2b exhibits the rate performances of all the samples at different current densities. The reversible capacity of the MoO$_3$/rGO-400 electrode is severely decreased from 734.9 to 110.1 mAh g^{-1} when the current density increases from 100 mA g^{-1} to 10 A g^{-1} (15.0% capacity retention), suggesting seriously limited Li$^+$ diffusion kinetics in MoO$_3$ at high current density.[16] In contrast, the capacity of the MoO$_3$@MoO$_2$/rGO-500 electrode decreased from 1312.6 to 795.8 mAh g^{-1} as the current density increased from 100 mA g^{-1} to 10 A g^{-1} (60.6% capacity retention). As the current returned to 100 mA g^{-1}, the capacity of 1187.4 mAh g^{-1} was still recovered. The excellent rate performance of the MoO$_3$@MoO$_2$/rGO-500 electrode indicates its high Li$^+$ diffusion coefficient, which was further confirmed by collecting CV curves at various scan rates from 0.5 to 10 mV s^{-1} (Figure S11a-c). Compared with MoO$_3$/rGO-400 and MoO$_2$/rGO-600, the shape of the CV curves of MoO$_3$@MoO$_2$/rGO-500 is well maintained, with a slight migration of the cathodic and anodic peaks at high scan rates, which implies a small amount of polarization.[37] The diffusion coefficient of Li$^+$ ions as they move in and out of the different electrodes was further estimated based on the following equation: $i_p = 2.686 \times 10^5 n^{3/2} A D^{1/2} c v^{1/2}$. (In which i_p, n, D, A, c, and v stand for the peak current, number of electrons, diffusion coefficient, surface area of the electrode, concentration

of Li^+, and voltage scanning rate, respectively). Apparently, the i_p exhibits a linear relationship with $v^{1/2}$, in which the slope is proportional to the diffusion coefficient (Figure S11d).[38] Thus, the diffusion coefficient for MoO$_3$/rGO-400 is relatively low. Compared with MoO$_2$/rGO-600, MoO$_3$@MoO$_2$/rGO-500 shows a higher diffusion coefficient, suggesting a good high-rate capability, possibly due to the importation of MoO$_2$ phase and the interfacial effects of the heterostructure.[39]

The cycling performances of the different electrodes at 2 A g^{-1} were measured (Figure 2c and Figure S12). The MoO$_3$@MoO$_2$/rGO and MoO$_2$/rGO electrodes show good cycling performance, with the capacity increasing in the initial few tens of cycles, and they maintain a constant capacity during the following cycles. The capacity of MoO$_3$/rGO-400 fades drastically after 30 cycles, however, and only 207.7 mAh g^{-1} of capacity is maintained after 200 cycles, which should possibly be ascribed to the pulverization issue. In the XRD pattern collected after 200 cycles (Figure S13), the MoO$_3$/rGO-400 pattern displays broad and weak peaks, which cannot be assigned to a specific crystalline phase of MoO$_x$ or Li$_x$MoO$_3$.[9] In particular, one of the dominant peaks at ~37.2° has shifted from 38.9° in the original XRD pattern of α-MoO$_3$ due to the volume expansion. The broad peak indicates that MoO$_3$/rGO-400 is incompletely amorphous, although the structure is disordered.[16] Although the MoO$_2$ peak of the MoO$_3$@MoO$_2$/rGO-500 electrode shows a slight shift to the left, MoO$_2$ still maintains its monoclinic structure even after 200 cycles, and a similar Mo 3d core level XPS spectrum with 3d^{4+} and 3d^{6+} still can be observed (Figure S14), suggesting high reversibility and structural stability for MoO$_2$. The core-shell structure with its MoO$_2$ shell will help to maintain the structural stability of the composite material, thus improving the cycling performance of the electrode. The MoO$_3$@MoO$_2$/rGO-500 electrode was subjected to prolonged cycling at 5 A g^{-1} (Figure 2d), and it delivered a high reversible capacity of 1208.9 mAh g^{-1} even after 2000 cycles, with a coulombic efficiency of 99.99%, demonstrating

fascinating high-rate cycling stability, which is very promising compared to the Mo-based anode materials reported so far, including MoO_{3-x},[27] MoO_{3-x}/carbon nanotube (CNT),[17] $MoO_3@TiO_2$,[16] MoO_2/C, and $MoO_2@rGO$,[20, 40] as presented in Figure 2e.

In order to deeply understand the electrical conductivity and interfacial effects produced by the creation of heterostructures and the *in-situ* importation of MoO_2, which may be responsible for the enhanced performance of the $MoO_3@MoO_2/rGO$-500 electrode, density functional theory (DFT) calculations were carried out to compare α-MoO_3 (Pbnm, $a = 3.963$, $b = 13.855$, $c = 3.696$ Å, as shown in Figure 3a) and MoO_2 (P21/c, $a = 5.610$, $b = 4.857$, $c = 5.626$ Å, as shown in Figure 3c), and explore the influence of their interface. Figure 3e reveals the densities of states (DOS) of orthorhombic α-MoO_3 and monoclinic MoO_2. The results shows that the region near the Fermi level of MoO_2 is mainly composed of Mo 3d orbitals, demonstrating a metallic character.[29] Whereas, the highest occupied states of α-MoO_3 are mostly composed of O 2p orbitals, and the Mo 3d orbitals of α-MoO_3 are not continuous at the Fermi level (with an obvious band gap for α-MoO_3, indicating its semiconducting nature).[26] The electron density differences in both materials were also plotted, as shown in Figure 3b and 3d, and it is clear that the valence electrons of Mo atoms are transferred to the O atoms in both materials. An obvious charge transfer in α-MoO_3 is observed between O and Mo atoms, reflecting the strong bonding between them, which endows the polar Mo-O bond with high stability.[34] In contrast, the abundant nonpolar Mo-Mo metallic bonds in MoO_2 enhance the conductivity. According to the above calculations, the partial transformation of MoO_3 to form $MoO_3@MoO_2$ heterostructures will effectively improve the electrical conductivity of the composite.

According to the solid-state reaction kinetics, α-MoO_3 is transformed to MoO_2 phase along the [010] direction. This reduction process causes the collapse of the successive (010) planes of MoO_3.[31] The <100> rows in MoO_2, during this transformation, constituted by strongly

linked elements (edge-sharing MoO_6 octahedra), are found to be arranged in some directions that are perpendicular or very oblique with respect to the initial (010) surface of MoO_3.[41] In this phase transformation process, the loss of $O_{(3)}$ lattice oxygen at the (010) facet of MoO_3 and the re-organization of lattice oxygen with increasing temperature generate the *n-p* heterojunctions of $MoO_3@MoO_2$ with abundant oxygen vacancies at the interface of MoO_3 and MoO_2 (Figure 3f), thereby providing more active sites for redox reactions, which make a greater contribution to the capacity of the electrode.[37, 42-44] DFT calculations were also performed to provide deeper insight into the interfacial effects on the electrochemical performance of the $MoO_3@MoO_2/rGO$-500 electrode (Figure 3g and Figure S15). Similar interface effects have been reported, which demonstrate that the mixed-phase interface not only offers abundant active sites for Li storage but also promotes the reaction kinetics by reducing the resistance.[14-15] In our case, the oxygen vacancies formed at the interface of MoO_3 and MoO_2 modify the charge distribution, leading to an unbalanced charge distribution and an interfacial electric field (visualized by the electron density difference map in Figure 3h), which results in a local in-built driving force.[24] These effects promote electron transport/ion diffusion at the interface, which synergistically leads to the high diffusion coefficient of Li^+ and high-rate performance of the $MoO_3@MoO_2/rGO$-500 electrode.

To fully understand the phase evolution during the charge/discharge process, in-operando synchrotron XRPD of the $MoO_3@MoO_2/rGO$-500 electrode was carried out (Figure 4a). Due to its possible preferred orientation, weak peak intensity, and the effects of the electrolyte and separator, the peaks of MoO_3 cannot be discerned explicitly (Figure S16a). During the discharge process, the (011) and (022) peaks of MoO_2 consecutively shift to lower angles, indicating the increase in the lattice parameter due to the intercalation of Li^+.[18] Then, both peaks are gradually converted into the (011) and (220) peaks of monoclinic $Li_{0.98}MoO_2$ when the potential reaches ~1.0 V, which is more distinct in the contour maps (Figure 4b).

Simultaneously, several new diffraction peaks located at 15.5° and 21.7° appear, corresponding to the ($\bar{0}$02) and (022) crystal planes of $Li_{0.98}MoO_2$ (Figure S17), which is consistent with the reaction mechanisms of MoO_2 (Figure 3a).[30] Importantly, a new diffraction peak at 17.9° is observed, which is ascribed to the (110) planes of Mo (Figure 4c), demonstrating a conversion reaction process. Remarkably, the (011) and (022) peaks of MoO_2 completely re-emerge, while the crystalline phase of $Li_{0.98}MoO_2$ disappears during the charge process, indicating that the crystallinity of the MoO_2 phase is well maintained after cycling. The high reversibility of the MoO_2 coating phase has benefits for the high-rate cycling stability of the MoO_3@MoO_2 heterostructures.

CONCLUSION

In summary, heterostructure manipulation was realized by an *in-situ* localized phase transformation route to synthesize the quasi-core-shell MoO_3@MoO_2 heterostructures anchored on rGO nanosheets. It was demonstrated that the outer MoO_2 phase improves the electrochemical performance due to the following reasons: a) the *in-situ* phase transformation at the boundary and surface not only improves the electronic conductivity of the MoO_3@MoO_2 heterostructures, but also shortens the Li^+ ion diffusion distance and electron transport in the inner MoO_3; b) a disproportionate charge distribution and lattice defects exist at the interface, which provide the force to boost the charge transfer kinetics on the interface and offer more active sites for Li^+ ion storage; and c) the quasi-core-shell structure helps to stabilize the structure of the active material. Consequently, the MoO_3@MoO_2/rGO-500 electrode delivers high reversible capacity (1312.6 mAh g^{-1} at 100 mA g^{-1}) and superior high-rate cycling performance (1208.9 mAh g^{-1} after 2000 cycles at 5 A g^{-1}). It is expected that our work can provide another way to optimize the transition metal oxides with heterostructures *via in-situ* localized phase transformation for high performance in optoelectronics, high-speed electronics, and other applications.

MATERIALS AND METHODS

Materials: $(NH_4)_6Mo_7O_{24}\cdot 4H_2O$ and graphite were purchased from Sigma-Aldrich Chemical Co. All other reagents were analytical grade and used directly without further purification.

Synthesis of MoO$_3$@MoO$_2$/rGO: The GO was prepared via a modified Hummers method. A colloidal GO solution with the concentration of about 2 mg mL^{-1} was prepared by ultrasonication (KQ-600KDE, 600 W) for 24 h. Subsequently, the colloidal GO solution was centrifuged to remove large GO particles at 5000 rpm for 5 min. $(NH_4)_6Mo_7O_{24}\cdot 4H_2O$ (2.0 g) was dissolved in distilled water (20 mL) to prepare a $(NH_4)_6Mo_7O_{24}$ solution. Subsequently, the $(NH_4)_6Mo_7O_{24}$ solution was added to 200 mL GO dispersion quickly under magnetic stirring for approximately 10 min. After drying in a vacuum freeze-drying oven, the solid–state precursor, $(NH_4)_6Mo_7O_{24}$/GO, was obtained. After that, a calcination procedure was carried out on the solid-state mixture with a given heating rate of 10 °C min^{-1} at target temperature of 400, 450, 500, 550, and 600 °C for 2 h in a tubular furnace (SK-G08123K, Φ100/92×1000 mm^2, under Ar atmosphere with a flow rate of 100 sccm). Finally, the black sheet-like products, denoted as MoO$_3$/rGO-400, MoO$_3$@MoO$_2$/rGO-450, MoO$_3$@MoO$_2$/rGO-500, MoO$_2$/rGO-550, and MoO$_2$/rGO-600 samples, respectively, were collected.

Materials characterization: The obtained materials were investigated by XRD with Cu Kα radiation at 1 °C min^{-1}. XPS measurements were performed on a VG Multilab 2000 (VG Inc.) photoelectron spectrometer by employing the monochromatic Al Kα radiation under vacuum at 2×10^{-6} Pa. The morphologies of the as-prepared MoO$_3$/rGO, MoO$_3$@MoO$_2$/rGO, and MoO$_2$/rGO sheets were observed by SEM (JEOL JSM-7500FA). The details of the crystal structure and energy dispersive spectroscopy (EDS) mapping were further examined by scanning TEM (STEM) (JEOL JEM-ARM200F), which was conducted at 80 kV. Atomic force microscopy was conducted *via* a Veeco DI Nano-scope MultiMode V system.

Continuous-wave EPR experiments were conducted on a Bruker ELEXSYS E580 spectrometer operating in the X-band (9.4 GHz) mode.

Electrochemical measurements: CR2032 coin-type cells were used to conduct the electrochemical tests, in which the working electrodes were prepared by mixing, Super P, poly(acrylic acid)/sodium carboxymethyl cellulose (1:1), and the obtained materials in a weight ratio of 10:10:80, dried at 80 °C in vacuum-oven for 12 h. 1 M $LiPF_6$ in ethylene carbonate/diethyl carbonate/dimethyl carbonate (1/1/1; v/v) with 5 wt% fluoroethylene carbonate was employed as the electrolyte. CV data were collected at different scan rates on a VMP-3 electrochemical workstation. The cells were galvanostatically charged-discharged with a voltage window of 0.01–3.0 V *versus* Li/Li^+ on the Neware battery tester at different current densities

In-operando synchrotron X-ray powder diffraction (XRPD): A synchrotron cell was used for in-operando XRPD measurements of $MoO_3@MoO_2$/rGO-500 sample, which is similar to the coin cells used in electrochemical testing. The cell was galvanostatically charged-discharged in 0.1–3.0 V (*vs.* Li^+/Li) at 0.18 mA (~200 mA g^{-1}). The XRPD patterns were collected every 3 min using a MYTHEN micro-strip detector during the charge-discharge process. The used wavelength was detected to be 0.6887 Å using a LaB_6 NIST SRM 660b (Australian Synchrotron).

Theoretical calculations: The Cambridge Serial Total Energy Package (CASTEP), a first-principles plane wave pseudopotential method based on the DFT, was employed to carry on all calculations. In order to achieve a good convergence of the total energy as well as force acting on the atoms, the cut-off energy of the plane wave basis, for all models, was set at 340 eV. Special points sampling integration over the Brillouin zone was used in the Monkhorst-Pack method with 5×5×5, 6×2×7, and 2×2×1 special k-point meshes for MoO_2 and MoO_3 crystal cells, and MoO_3(010)/MoO_2(100) heterointerface models, respectively.

As experimentally determined, MoO_3 exhibits the orthorhombic structure with space group Pbnm. Its unit cell contains four formula units with the lattice constants of a = 3.963, b = 13.855, and c = 3.696 Å, as shown in Figure S13. As experimentally determined, MoO_2 presents the monoclinic structure with space group P21/c, and the unit cell contains two formula units with the lattice constants a = 5.610 Å, b = 4.857 Å, and c = 5.626 Å, as shown in Figure S2. To simulate the interface of $MoO_3(010)/MoO_2(100)$, an α-MoO_3 (010) (3 × 3) slab with 8 atomic layers was constructed to match with a MoO_2 (100) (2 × 2) slab with 6 atomic layers by keeping the thickness of the layers constant, as shown in Figure S14. A vacuum thickness of 20 Å was set to avoid interaction between neighboring slabs. The average lattice constants of the constructed $MoO_3(010)/MoO_2(100)$ heterointerface were a = 10.4012 Å and b = 11.5680 Å.

ASSOCIATED CONTENT

Supporting Information. The Supporting Information is available free of charge on the ACS Publications website at http://pubs.acs.org.

REFERENCES

1.   Hong, X.; Kim, J.; Shi, S.-F.; Zhang, Y.; Jin, C.; Sun, Y.; Tongay, S.; Wu, J.; Zhang, Y.; Wang, F., Ultrafast Charge Transfer in Atomically Thin MoS_2/WS_2 Heterostructures. Nat. Nanotechnol. **2014,** *9*, 682.

2.   Chen, C.; Xie, X.; Anasori, B.; Sarycheva, A.; Makaryan, T.; Zhao, M.; Urbankowski, P.; Miao, L.; Jiang, J.; Gogotsi, Y., MoS_2-on-Mxene Heterostructures as Highly Reversible Anode Materials for Lithium-Ion Batteries. Angew. Chem. Int. Ed. **2018,** *57*, 1846-1850.

3.   Pentcheva, R.; Pickett, W. E., Charge Localization or Itineracy at $LaAlO_3/SrTiO_3$ Interfaces: Hole Polarons, Oxygen Vacancies, and Mobile Electrons. Phys. Rev. B. **2006,** *74*, 035112.

4.   Gautam, U. K.; Fang, X.; Bando, Y.; Zhan, J.; Golberg, D., Synthesis, Structure, and Multiply Enhanced Field-Emission Properties of Branched ZnS Nanotube−in Nanowire Core−Shell Heterostructures. ACS Nano **2008,** *2*, 1015-1021.

5.   Sata, N.; Eberman, K.; Eberl, K.; Maier, J., Mesoscopic Fast Ion Conduction in Nanometre-Scale Planar Heterostructures. Nature **2000,** *408*, 946.

6.   Fang, Y.; Lv, Y.; Gong, F.; Elzatahry, A. A.; Zheng, G.; Zhao, D., Synthesis of 2D-Mesoporous-Carbon/MoS_2 Heterostructures with Well-Defined Interfaces for High-Performance Lithium-Ion Batteries. Adv. Mater. **2016,** *28*, 9385-9390.

7.   Liu, Y. T.; Zhang, P.; Sun, N.; Anasori, B.; Zhu, Q. Z.; Liu, H.; Gogotsi, Y.; Xu, B., Self-Assembly of Transition Metal Oxide Nanostructures on Mxene Nanosheets for Fast and Stable Lithium Storage. Adv. Mater. **2018,** *30*, 1707334.

8.   Mai, L. Q.; Hu, B.; Chen, W.; Qi, Y.; Lao, C.; Yang, R.; Dai, Y.; Wang, Z. L., Lithiated MoO_3 Nanobelts with Greatly Improved Performance for Lithium Batteries. Adv. Mater. **2007**, 19, 3712-3716.

9.   Lee, S. H.; Kim, Y. H.; Deshpande, R.; Parilla, P. A.; Whitney, E.; Gillaspie, D. T.;

Jones, K. M.; Mahan, A. H.; Zhang, S.; Dillon, A. C., Reversible Lithium-Ion Insertion in Molybdenum Oxide Nanoparticles. Adv. Mater. 2008, 20, 3627-3632.

10.   Choi, S. H.; Kang, Y. C., Crumpled Graphene-Molybdenum Oxide Composite Powders: Preparation and Application in Lithium-Ion Batteries. ChemSusChem **2014,** *7*, 523-528.

11.   Zhu, C. B.; Usiskin, R. E.; Yu, Y.; Maier, J., The Nanoscale Circuitry of Battery Electrodes. Science **2017,** *358,* 2808.

12.   Wang, S.; Zhang, H. J.; Zhang, D.; Ma, Y.; Bi, X. F.; Yang, S. B., Vertically Oriented Growth of MoO_3 Nanosheets on Graphene for Superior Lithium Storage. J. Mater. Chem. A. **2018,** *6*, 672-679.

13.   Cheng, X. P.; Li, Y. H.; Sang, L. J.; Ma, J. Y.; Shi, H. F.; Liu, X. Q.; Lu, J. X.; Zhang, Y. F., Boosting the Electrochemical Performance of MoO_3 Anode for Long-Life Lithium Ion Batteries: Dominated by an Ultrathin TiO_2 Passivation Layer. Electrochim. Acta **2018,** *269*, 241-249.

14.   Zheng, Y.; Zhou, T. F.; Zhang, C. F.; Mao, J. F.; Liu, H. K.; Guo, Z. P., Boosted Charge Transfer in SnS/SnO_2 Heterostructures: Toward High Rate Capability for Sodium-Ion Batteries. Angew. Chem. Int. Ed. **2016,** *55*, 3408-3413.

15.   Kim, H. S.; Cook, J. B.; Lin, H.; Ko, J. S.; Tolbert, S. H.; Ozolins, V.; Dunn, B., Oxygen Vacancies Enhance Pseudocapacitive Charge Storage Properties of MoO_{3-X}. Nat. Mater. **2017,** *16*, 454.

16.   Wang, C.; Wu, L. X.; Wang, H.; Zuo, W. H.; Li, Y. Y.; Liu, J. P., Fabrication and Shell Optimization of Synergistic TiO_2-MoO_3 Core-Shell Nanowire Array Anode for High Energy and Power Density Lithium-Ion Batteries. Adv. Funct. Mater. **2015,** *25*, 3524-3533.

17.   Ni, J. F.; Wang, G. B.; Yang, J.; Gao, D. L.; Chen, J. T.; Gao, L. J.; Li, Y., Carbon Nanotube-Wired and Oxygen-Deficient MoO_3 Nanobelts with Enhanced Lithium-Storage

Capability. J. Power Sources **2014,** *247*, 90-94.

18. Sun, Y. M.; Hu, X. L.; Luo, W.; Huang, Y. H., Self-Assembled Hierarchical MoO_2/Graphene Nanoarchitectures and Their Application as a High-Performance Anode Material for Lithium-Ion Batteries. ACS Nano **2011,** *5*, 7100-7107.

19. Balendhran, S.; Deng, J. K.; Ou, J. Z.; Walia, S.; Scott, J.; Tang, J. S.; Wang, K. L.; Field, M. R.; Russo, S.; Zhuiykov, S.; Strano, M. S.; Medhekar, N.; Sriram, S.; Bhaskaran, M.; Kalantar-Zadeh, K., Enhanced Charge Carrier Mobility in Two-Dimensional High Dielectric Molybdenum Oxide. Adv. Mater. **2013,** *25*, 109-114.

20. Wang, P. X.; Zhang, Y.; Yin, Y. Y.; Fan, L. S.; Zhang, N. Q.; Sun, K. N., Anchoring Hollow MoO_2 Spheres on Graphene for Superior Lithium Storage. Chem. Eng. J. **2018,** *334*, 257-263.

21. Liu, Y. T.; Zhang, P.; Sun, N.; Anasori, B.; Zhu, Q. Z.; Liu, H.; Gogotsi, Y.; Xu, B., Self-Assembly of Transition Metal Oxide Nanostructures on Mxene Nanosheets for Fast and Stable Lithium Storage. Adv. Mater. **2018,** *30,*1707334.

22. Zhou, T. F.; Zheng, Y.; Gao, H.; Min, S. D.; Li, S.; Liu, H. K.; Guo, Z. P., Surface Engineering and Design Strategy for Surface-Amorphized TiO_2@Graphene Hybrids for High Power Li-Ion Battery Electrodes. Adv. Sci. **2015,** *2,* 1500027.

23. Smith, A. M.; Lane, L. A.; Nie, S. M., Mapping the Spatial Distribution of Charge Carriers in Quantum-Confined Heterostructures. Nat. Commun. **2014,** *5,* 4506.

24. Basletic, M.; Maurice, J. L.; Carretero, C.; Herranz, G.; Copie, O.; Bibes, M.; Jacquet, E.; Bouzehouane, K.; Fusil, S.; Barthelemy, A., Mapping the Spatial Distribution of Charge Carriers in $LaAlO_3$/$SrTiO_3$ Heterostructures. Nat. Mater. **2008,** *7*, 621-625.

25. Ni, J. F.; Zhao, Y.; Li, L.; Mai, L. Q., Ultrathin MoO_2 Nanosheets for Superior Lithium Storage. Nano Energy **2015,** *11*, 129-135.

26. Shon, J. K.; Lee, H. S.; Park, G. O.; Yoon, J.; Park, E.; Park, G. S.; Kong, S. S.; Jin,

M.; Choi, J. M.; Chang, H.; Doo, S.; Kim, J. M.; Yoon, W. S.; Pak, C.; Kim, H.; Stucky, G. D., Discovery of Abnormal Lithium-Storage Sites in Molybdenum Dioxide Electrodes. Nat. Commun. **2016,** *7,* 11049.

27.   Zhang, G.; Xiong, T.; Yan, M.; He, L.; Liao, X.; He, C.; Yin, C.; Zhang, H.; Mai, L., α-MoO_{3-X} by Plasma Etching with Improved Capacity and Stabilized Structure for Lithium Storage. Nano Energy **2018,** *49*, 555-563.

28.   Wang, W.; Qin, J.; Yin, Z.; Cao, M., Achieving Fully Reversible Conversion in MoO_3 for Lithium Ion Batteries by Rational Introduction of $CoMoO_4$. ACS Nano **2016,** *10*, 10106-10116.

29.   Scanlon, D. O.; Watson, G. W.; Payne, D. J.; Atkinson, G. R.; Egdell, R. G.; Law, D. S. L., Theoretical and Experimental Study of the Electronic Structures of MoO_3 and MoO_2. J. Phys. Chem. C **2010,** *114*, 4636-4645.

30.   Ren, Y.; Armstrong, A. R.; Jiao, F.; Bruce, P. G., Influence of Size on the Rate of Mesoporous Electrodes for Lithium Batteries. J. Am. Chem. Soc. **2010,** *132*, 996-1004.

31.   Ressler, T.; Wienold, J.; Jentoft, R. E.; Neisius, T., Bulk Structural Investigation of the Reduction of MoO_3 with Propene and the Oxidation of MoO_2 with Oxygen. J. Catal. **2002,** *210*, 67-83.

32.   Liu, Y. W.; Zhou, T. F.; Zheng, Y.; He, Z. H.; Xiao, C.; Pang, W. K.; Tong, W.; Zou, Y. M.; Pan, B. C.; Guo, Z. P.; Xie, Y., Local Electric Field Facilitates High-Performance Li-Ion Batteries. ACS Nano **2017,** *11*, 8519-8526.

33.   Lalik, E., Kinetic Analysis of Reduction of MoO_3 to MoO_2. Catal. Today **2011,** *169*, 85-92.

34.   Janotti, A.; Van de Walle, C. G., Oxygen Vacancies in ZnO. Appl. Phys. Lett. 2005, 87, 122102.

35.   Wang, P. F.; Yao, H. R.; Liu, X. Y.; Yin, Y. X.; Zhang, J. N.; Wen, Y. R.; Yu, X. Q.;

Gu, L.; Guo, Y. G., Na$^+$/Vacancy Disordering Promises High-Rate Na-Ion Batteries. Sci. Adv. **2018,** *4,* 6018.

36.　　Zhang, P.; Zou, L.; Hu, H. X.; Wang, M. R.; Fang, J.; Lai, Y. Q.; Li, J., 3d Hierarchical Carbon Microflowers Decorated with MoO_2 Nanoparticles for Lithium Ion Batteries. Electrochim. Acta **2017,** *250,* 219-227.

37.　　Shin, J. Y.; Joo, J. H.; Samuelis, D.; Maier, J., Oxygen-Deficient TiO_2-Delta Nanoparticles Via Hydrogen Reduction for High Rate Capability Lithium Batteries. Chem. Mater. **2012,** *24,* 543-551.

38.　　Gao, H.; Zhou, T.; Zheng, Y.; Zhang, Q.; Liu, Y.; Chen, J.; Liu, H.; Guo, Z., Cos Quantum Dot Nanoclusters for High Energy Potassium Ion Batteries. Adv. Funct. Mater. **2017,** *27,* 1702634.

39.　　Zheng, Y.; Zhou, T. F.; Zhao, X. D.; Pang, W. K.; Gao, H.; Li, S.; Zhou, Z.; Liu, H. K.; Guo, Z. P., Atomic Interface Engineering and Electric-Field Effect in Ultrathin Bi_2MoO_6 Nanosheets for Superior Lithium Ion Storage. Adv. Mater. **2017,** *29,* 1700396.

40.　　Tian, W.; Hu, H.; Wang, Y. X.; Li, P.; Liu, J. Y.; Liu, J. L.; Wang, X. B.; Xu, X. D.; Li, Z. T.; Zhao, Q. S.; Ning, H.; Wu, W. T.; Wu, M. B., Metal-Organic Frameworks Mediated Synthesis of One-Dimensional Molybdenum-Based/Carbon Composites for Enhanced Lithium Storage. ACS Nano **2018,** *12,* 1990-2000.

41.　　Bertrand, O.; Dufour, L. C., X-Ray and Electron-Microscopy Investigation of the Topotactic Transformation of MoO_3 into MoO_2. Phys. Status Solidi A **1980,** *60,* 507-519.

42.　　Xu, Y.; Zhou, M.; Wang, X.; Wang, C. L.; Liang, L. Y.; Grote, F. B.; Wu, M. H.; Mi, Y.; Lei, Y., Enhancement of Sodium Ion Battery Performance Enabled by Oxygen Vacancies. Angew. Chem. Int. Ed. **2015,** *54,* 8768-8771.

43.　　Greiner, M. T.; Lu, Z.H., Thin-film Metal Oxides in Organic Semiconductor Devices: Their Electronic Structures, Work Functions and Interfaces. NPG Asia Mater. 2013, 5, 55.

44 . Ratna Phani, A.; Manorama, S.; Rao, V., Effect of Additives on the Response of Sensors Utilizing Semiconducting Oxide on Carbon Monoxide Sensitivity. Appl. Phys. Lett. 1995, 66, 3489-3491.
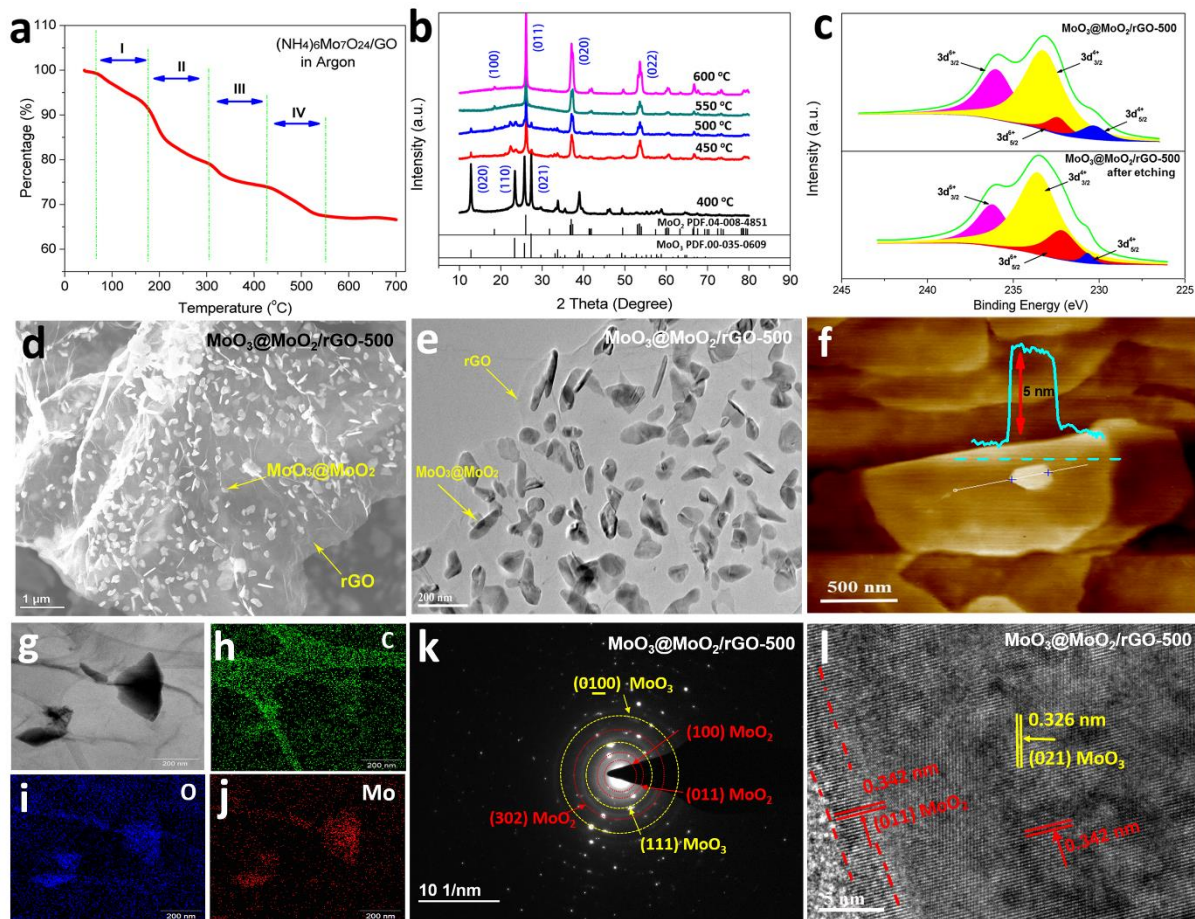
Figure 1. Crystal structure, compositional characterization, and morphology of MoO$_3$@ MoO$_2$/rGO sheets. (a) TGA curve of precursor, (NH$_4$)$_6$Mo$_7$O$_{24}$/GO, under calcining from ambient temperature to 700 °C in argon. (b) XRD patterns of the different samples obtained at various temperatures (from 400 to 600 °C). (c) High-resolution XPS spectra of MoO$_3$@MoO$_2$/rGO-500 sample before and after argon plasma etching. (d) SEM image of MoO$_3$@MoO$_2$/rGO-500 nanosheets. (e) TEM image of MoO$_3$@MoO$_2$/rGO-500 nanosheets. (f) Atomic force microscope (AFM) image of MoO$_3$@MoO$_2$/rGO-500 and corresponding height profile. (g–j) Scanning TEM (STEM) image with corresponding energy dispersive spectroscopy (EDS) elemental mappings. (k) The selected area electron diffraction (SAED) pattern of MoO$_3$@MoO$_2$/rGO-500 sample with complex polycrystalline diffraction spots that correspond to the monoclinic MoO$_2$ and α-MoO$_3$ phases. (l) HRTEM image of MoO$_3$@MoO$_2$/rGO-500 sample. Two kinds of lattice spacing can be observed.
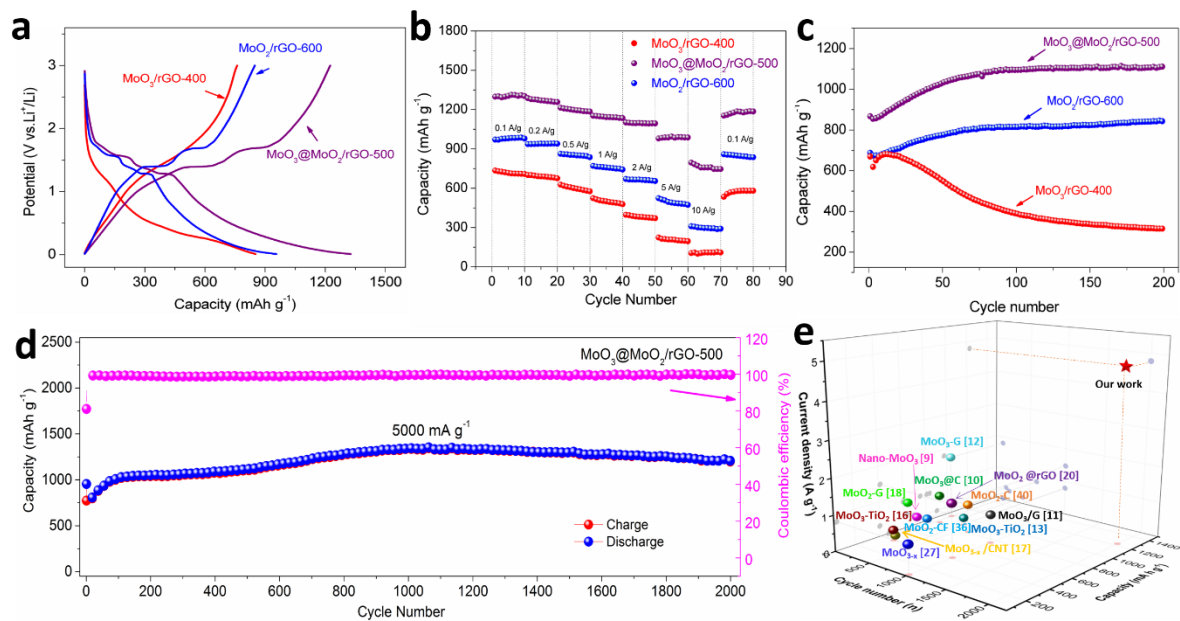
Figure 2. Electrochemical performance of different electrodes. (a) Typical galvanostatic discharge-charge profiles of MoO_3/rGO-400, $MoO_3@MoO_2/rGO$-500, and MoO_2/rGO-600 electrodes at 100 mA g^{-1}. (b) Rate performances of MoO_3/rGO-400, $MoO_3@MoO_2/rGO$-500, and MoO_2/rGO-600 electrodes at current densities from 100 mA g^{-1} to 10 A g^{-1}. (c) Cycling performances of MoO_3/rGO-400, $MoO_3@MoO_2/rGO$-500, and MoO_2/rGO-600 electrodes at 2 A g^{-1}. (d) Long-term high-rate cycling performance of the $MoO_3@MoO_2/rGO$-500 electrode and the corresponding coulombic efficiency at 5 A g^{-1}. (e) Comparison of the high-rate cycling performance of the $MoO_3@MoO_2/rGO$-500 electrode with other reported Mo-based anodes in LIBs.
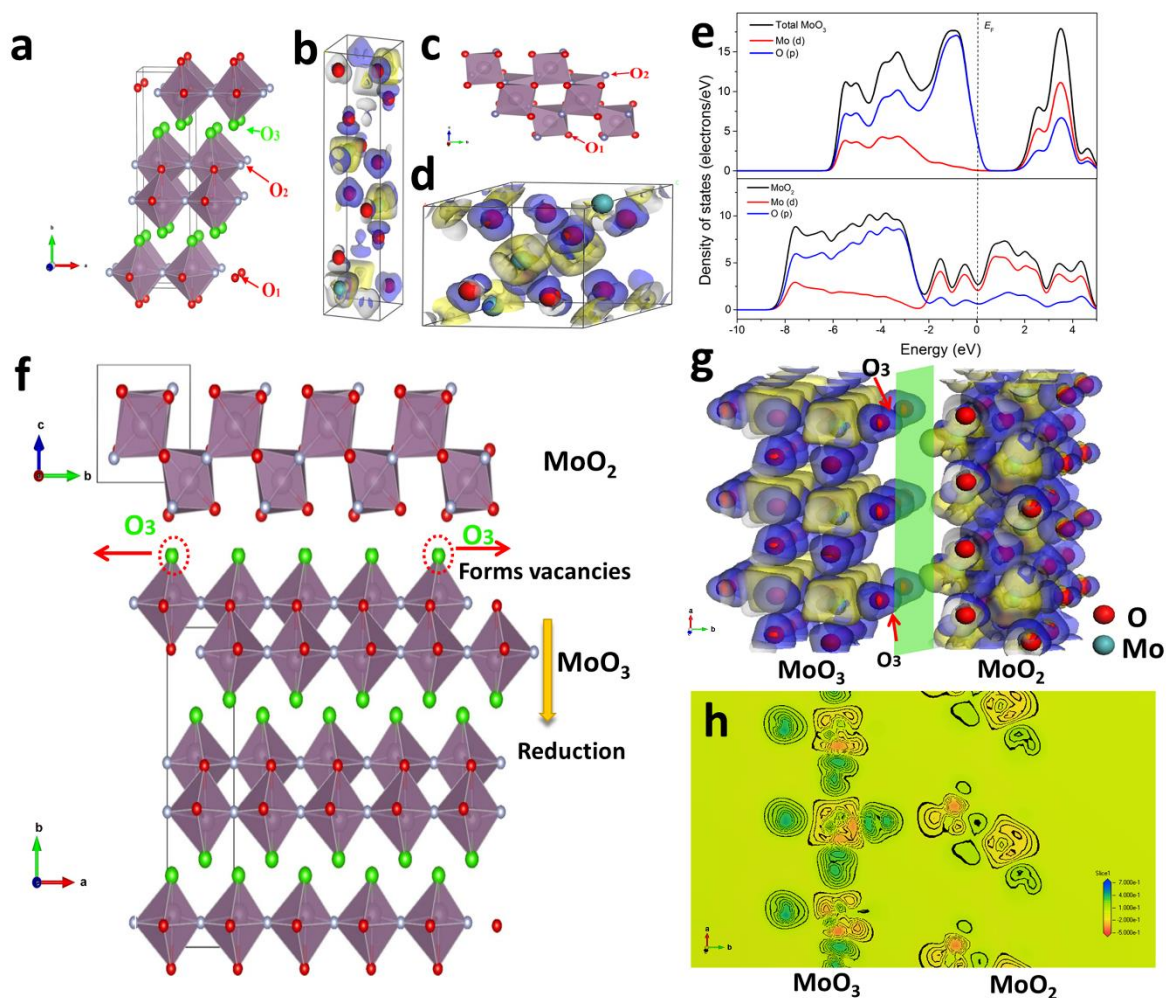
Figure 3. Structural information, in-situ phase transformation, and charge density distribution of MoO₃@MoO₂ heterostructures. (a) The crystal structure of α-MoO₃ with a bilayer network of edge-sharing MoO₆ octahedra. There are three nonequivalent oxygen atoms: (i) asymmetric oxygens, $O_{(1)}$, that bridge two Mo centers along the z axis; (ii) three coordinated oxygens, $O_{(2)}$, that form a symmetrical bridge along the x axis between two Mo centers on the same layer and interact with a sublayer Mo; and (iii) terminal oxygens, $O_{(3)}$, which are double bonded to only one Mo center that is present in the interlayer region. (b) Electron density differences for orthorhombic MoO₃ (c) The structure of monoclinic MoO₂. (d) Electron density differences for MoO₂. (e) Comparison of densities of states of MoO₃ and MoO₂. (f) Schematic representation of the in-situ phase transformation to form MoO₃@MoO₂

heterostructures. (g) Model for the interface of a MoO_3@MoO_2 heterostructure with oxygen vacancies. (h) Electron density difference map of the interface of a MoO_3@MoO_2 heterostructure.
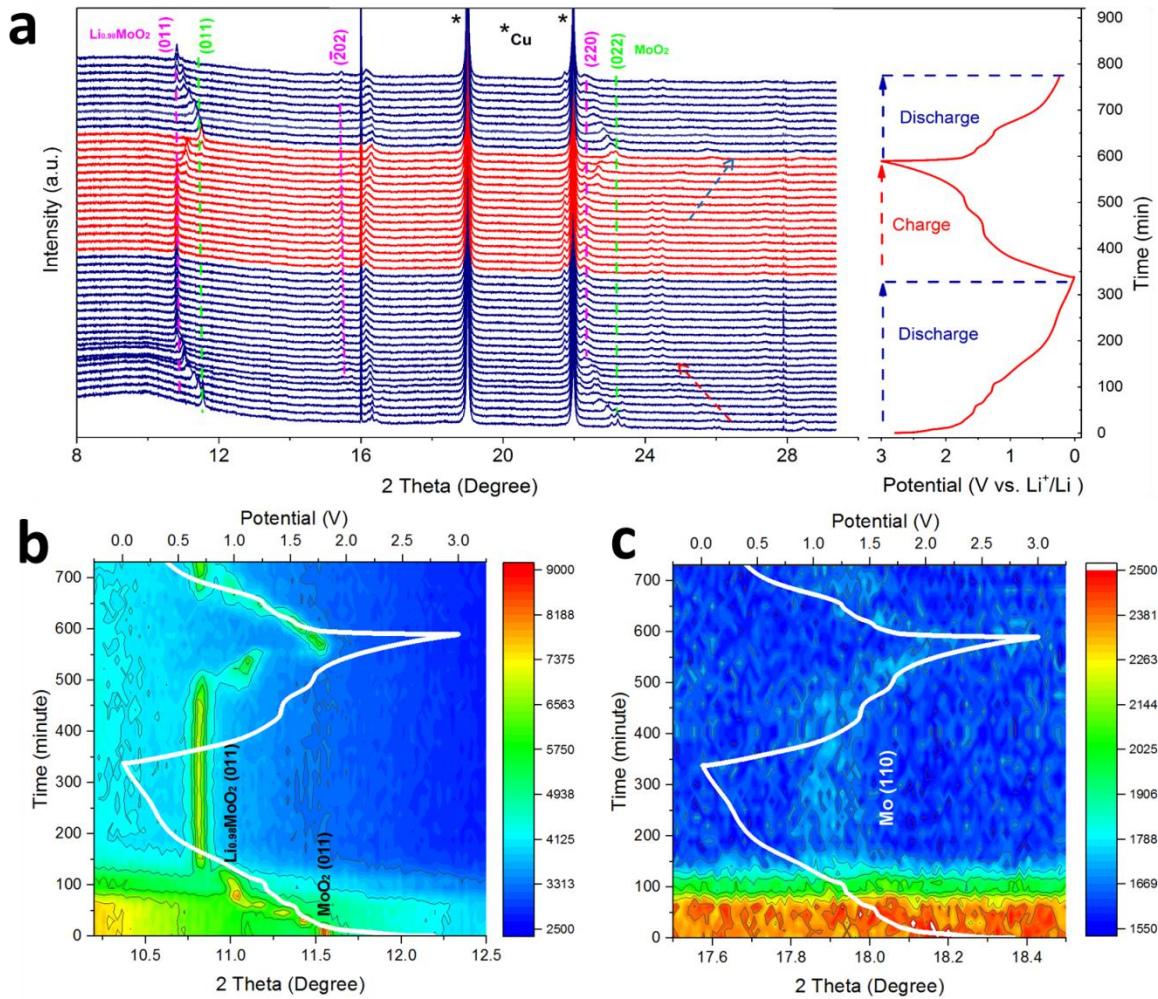
Figure 4. Crystal structural evolution under the Li⁺ (de)intercalation process. (a) In-operando synchrotron XRPD patterns of the $MoO_3@MoO_2/rGO$-500 electrode were collected during the initial discharge-charge process at 200 mA g^{-1}. Contour plots of the operando synchrotron XRPD data: (b) 10.0°−12.5°, where the (011) peak of MoO_2 is converted to the (011) peak of $Li_{0.98}MoO_2$ during the initial discharge process; (c) 17.5°−18.5°, where the peak of Mo can be observed at about 17.9°, demonstrating the partial conversion of $MoO_3@MoO_2$ heterostructures into Mo in the discharging process.

Supporting Information

Heterostructure Manipulation *via In-Situ* Localized Phase Transformation for High-Rate and Highly Durable Lithium Ion Storage

Junnan Hao[†], Jian Zhang[‡], Guanglin Xia [†], Yajie Liu[†], Yang Zheng[†], Wenchao Zhang[†], Yongbing Tang[* §], Wei Kong Pang[†], Zaiping Guo*[†]

[†] Institute for Superconducting & Electronic Materials, School of Mechanical, Materials and Mechatronics Engineering, University of Wollongong, Wollongong, NSW 2522, Australia

[‡] College of Automotive and Mechanical Engineering, Changsha University of Science and Technology, Changsha 410114, China

[§] Functional Thin Films Research Center; Shenzhen Institutes of Advanced Technology, Chinese Academy of Sciences, Shenzhen 518055, China

	400 °C	500 °C	500 °C etching	600 °C	Peak position (eV)
Mo^{+6} $_{5/2}$	63. 26%	5.01%	16.13%	3.62%	232.3
Mo^{+6} $_{3/2}$	33.74%	28.40%	23.69%	10.01%	236.1
Mo^{+4} $_{5/2}$	0	6.25%	2.05%	31.16%	230.7
Mo^{+4} $_{3/2}$	0	60.34%	58.13%	55.21%	233.5

Table S1. The positions of the 3d Mo^{6+} and 3d Mo^{4+} peaks in the XPS spectra of Mo 3d and their related contents in various samples.
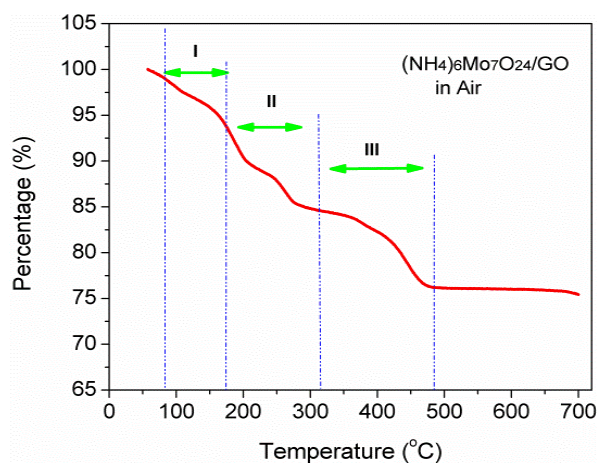
Figure S1. TGA curves of the $(NH_4)_6Mo_7O_{24}$/GO precursor, tested in air flow from ambient temperature to 700 °C. There are three obvious weight loss regions: the first (50–180 °C) and the second regions (180–310 °C) originate from the removal of the remaining interlayer moisture and the decomposition of $(NH_4)_6Mo_7O_{24}$, respectively. The following loss at approximately 300–420 °C is due to the oxidative decomposition reaction of GO sheets. As a result, the content of rGO in the composite was found to be ~6.8 wt%.[1]
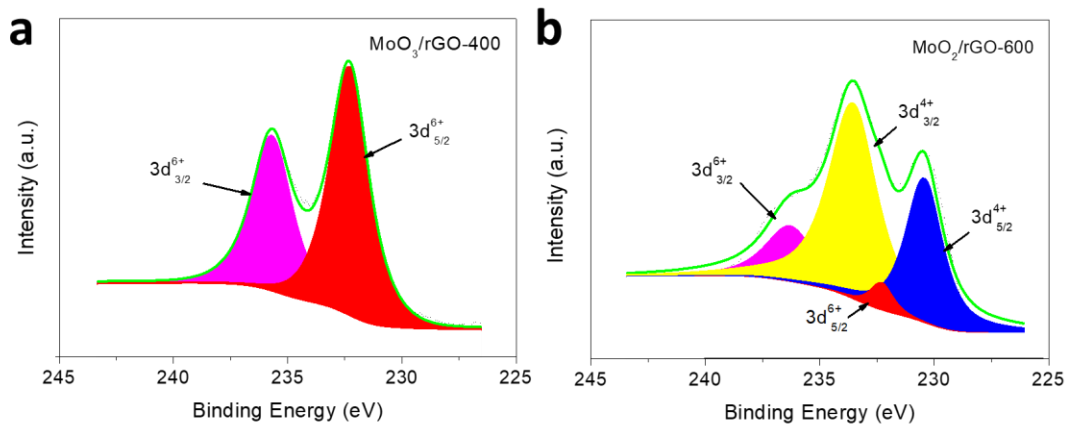
Figure S2. High-resolution XPS spectra of MoO_3/rGO-400 (a) and MoO_2/rGO-600 (b) sheets in the Mo 3d region.
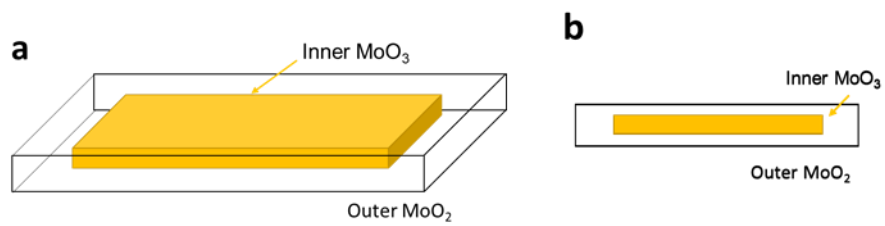
Figure S3. (a) Schematic illustration of $MoO_3@MoO_2$ heterostructures, (b) lateral view.
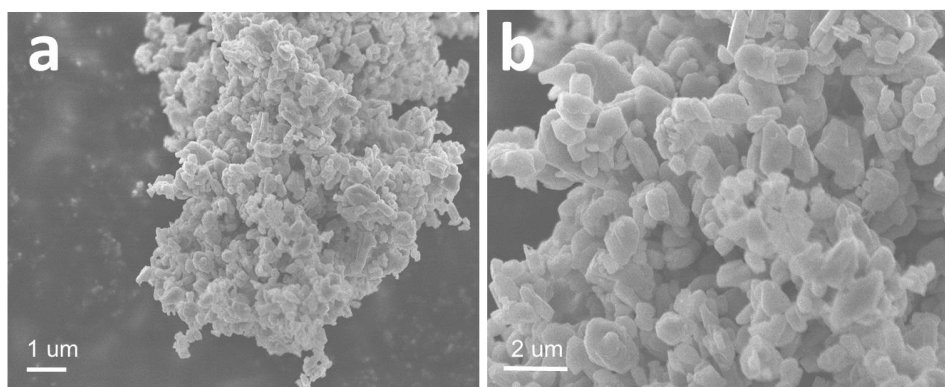
Figure S4. (a, b) SEM images of MoO_3@MoO_2-500 sample without rGO at different magnifications. It is clear that the MoO_3@MoO_2 heterostructure particles suffer from serious aggregation without rGO support.
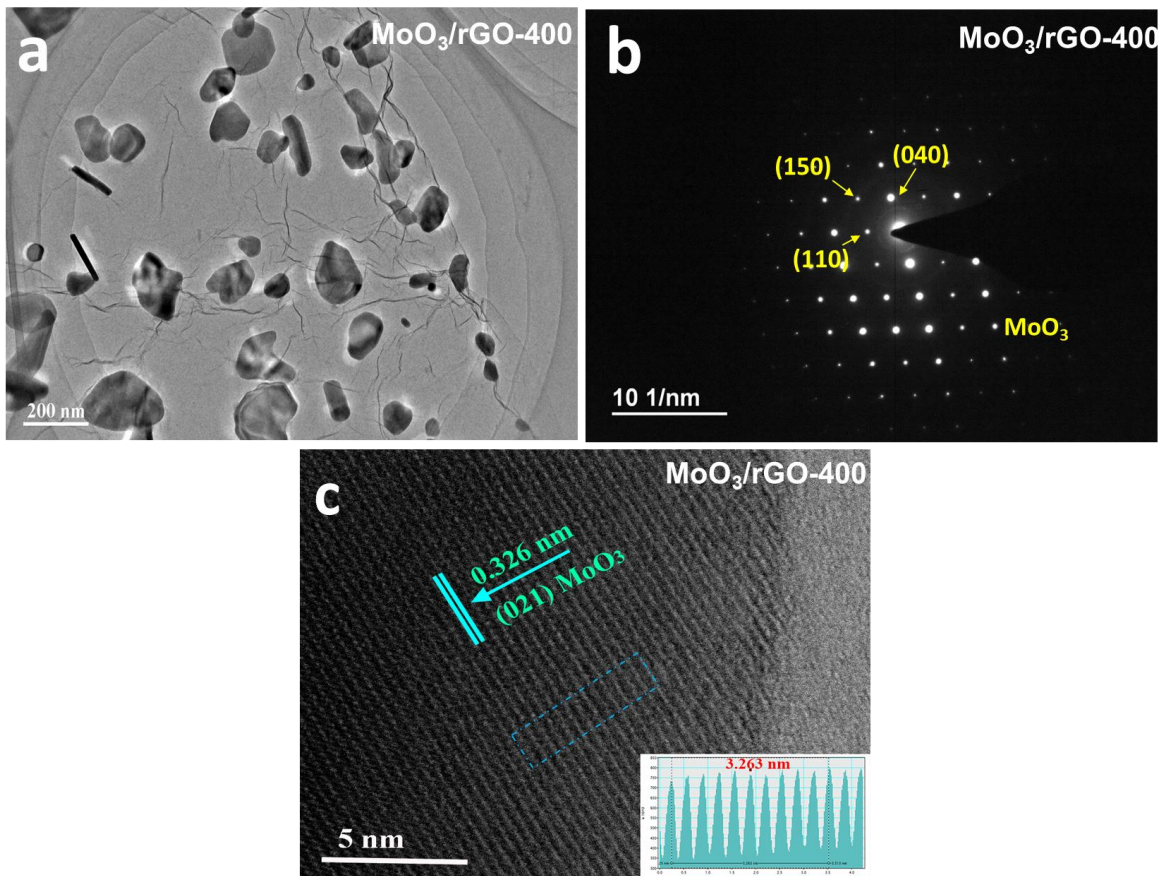
Figure S5. Morphology of MoO$_3$/rGO-400 sheets. (a) TEM image of MoO$_3$/rGO-400 sheets. (b) SAED pattern of the MoO$_3$/rGO-400 sample with the zone axis of [00-1]. (c) HRTEM image of MoO$_3$/rGO-400 sample (inset: measurement of the lattice spacing, evaluated as 0.326 nm).
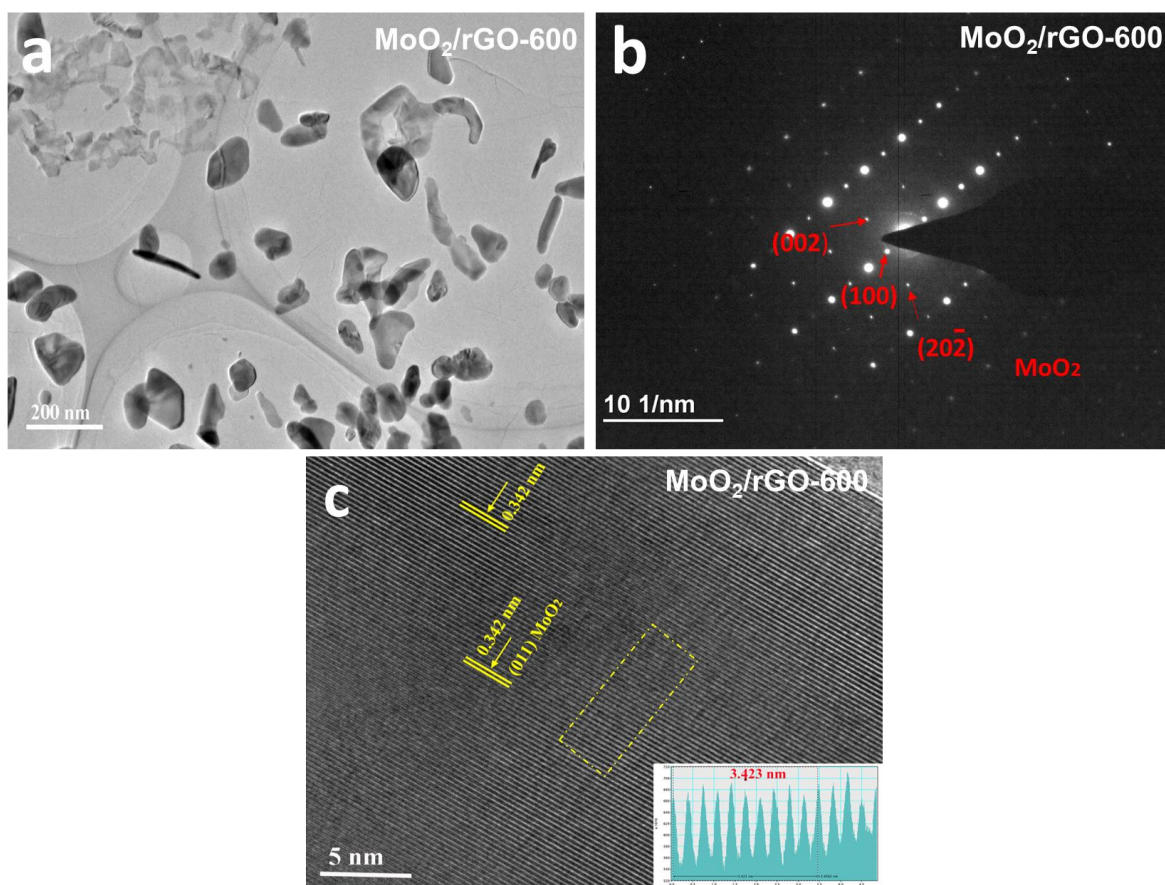
Figure S6. Morphology of MoO$_2$/rGO-600 sheets. (a) TEM image of MoO$_2$/rGO-600 sheets. (b) SAED pattern of MoO$_2$/rGO-600 sample. (c) HRTEM image of MoO$_2$/rGO-600 sample (inset: measurement of lattice spacing, evaluated as 0.342 nm).
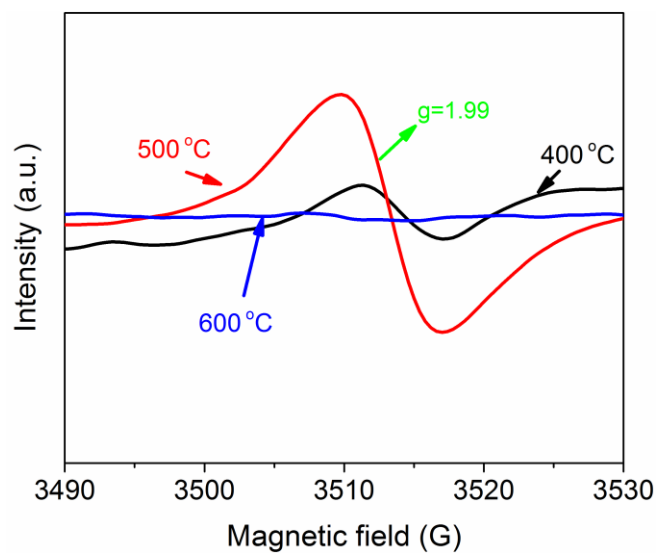
Figure S7. Electron paramagnetic resonance (EPR) spectrum of MoO_3/rGO-400, $MoO_3@MoO_2$/rGO-500, and MoO_2/rGO-600 samples.
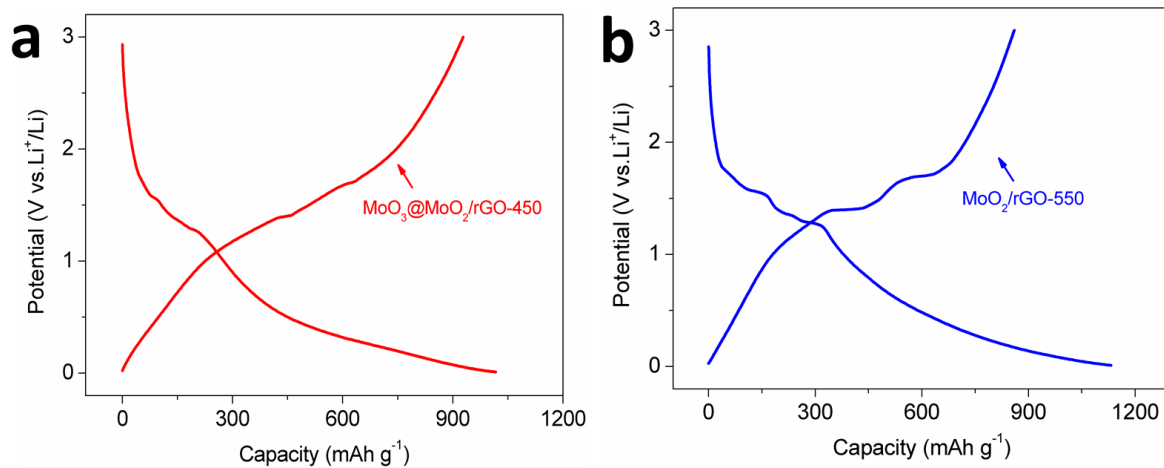
Figure S8. Typical galvanostatic discharge-charge profiles: (a) $MoO_3@MoO_2/rGO$-450, (b) MoO_2/rGO-550 electrodes.
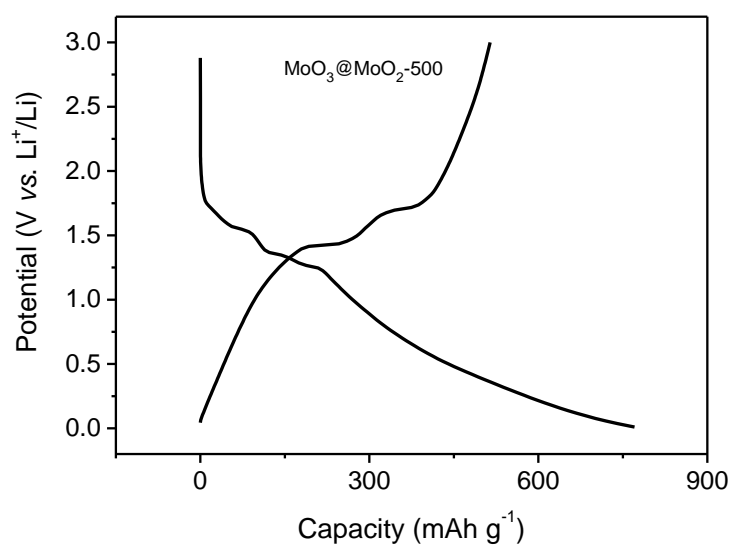
Figure S9. Typical charge-discharge curves of the $MoO_3@MoO_2$-500 without rGO. The discharge capacity of the $MoO_3@MoO_2$-500 electrode is much lower than that with rGO.
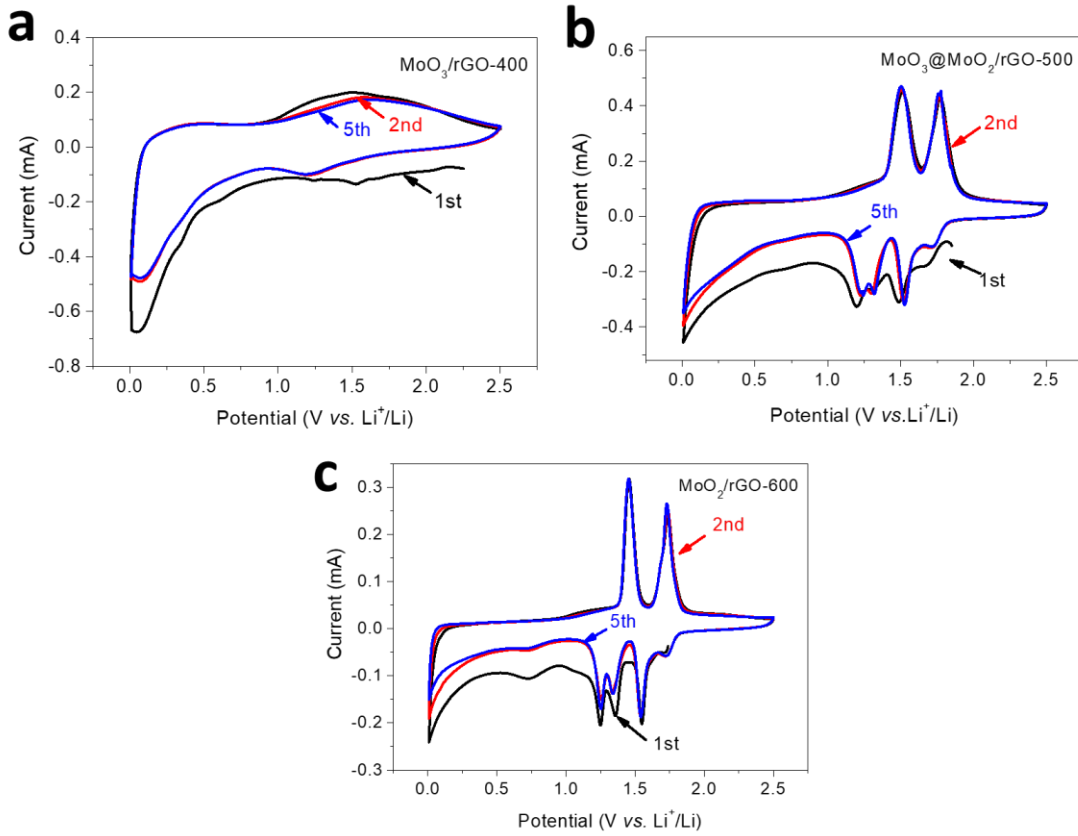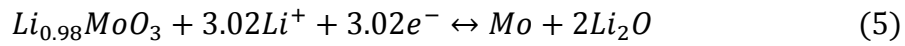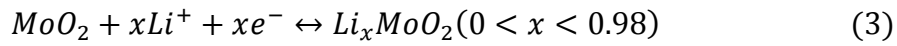
Figure S10. Cyclic voltammograms for the first, second, and fifth cycles: (a) MoO_3/rGO-400, (b) $MoO_3@MoO_2/rGO$-500, and (c) MoO_2/rGO-600 electrodes.

The cyclic voltammograms (CVs) of different samples for the first, second, and fifth cycles were collected at 0.5 mV s^{-1}. In the first cycle of MoO_3/rGO-400 (Figure S6a), two broad and weak peaks at around 1.52 and 1.25 V are visible, corresponding to the intercalation of Li$^+$ into [MoO_6] bi-layers to form Li_xMoO_3 (x_{max} = 1.5). In the subsequent lithiation process, another sharp peak appears below 0.4 V, corresponding to the conversion reaction of Li_xMoO_3.[2] Overall, the Li storage reaction in MoO_3 can be described as follows:

$$MoO_3 + xLi^+ + xe^- \leftrightarrow Li_xMoO_3 (0 < x < 1.5) \qquad (1)$$

$$Li_xMoO_3 + (6 - x)Li^+ + (6 - x)e^- \leftrightarrow Mo + 3Li_2O \qquad (2)$$

11
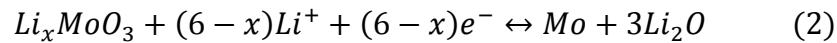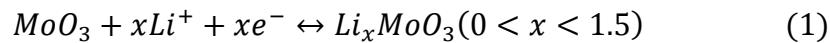
Due to the presence of MoO_2, the CV curves of $MoO_3@MoO_2/rGO$-500 and MoO_2/rGO-600 are different from that of MoO_3/rGO-400 electrode. Three sharp reduction peaks located at approximately 1.25, 1.31, and 1.52 V can be observed (Figure S6b and S6c), which mainly arise from the phase transitions from the original monoclinic to the orthorhombic phase and then from the orthorhombic to the monoclinic phase in the Li insertion process.[3] The reaction mechanism of MoO_2 can be described as follows:
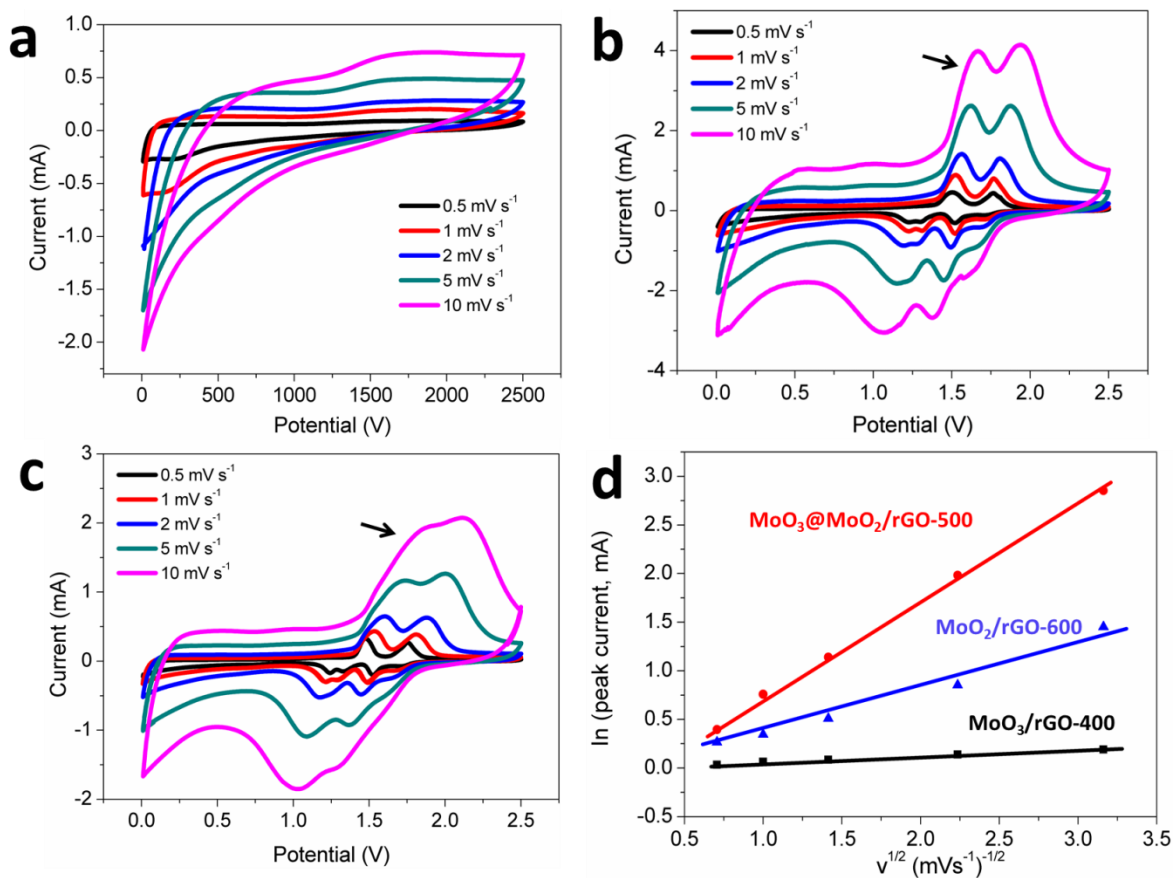
$$MoO_2 + xLi^+ + xe^- \leftrightarrow Li_xMoO_2 (0 < x < 0.98) \qquad (3)$$

$$Li_xMoO_2 + yLi^+ + ye^- \leftrightarrow Li_{(x+y)}MoO_2 (0 < x, y < 0.98) \qquad (4)$$

$$Li_{0.98}MoO_3 + 3.02Li^+ + 3.02e^- \leftrightarrow Mo + 2Li_2O \qquad (5)$$
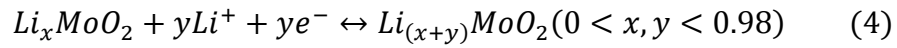
Figure S11. CV curves at various scan rates: (a) MoO$_3$/rGO-400 electrode, (b) MoO$_3$@MoO$_2$/rGO-500 electrode, (c) MoO$_2$/rGO-600 electrode. (d) The linear relationship between the peak current (i_p) and the square root of the scan rate ($v^{1/2}$) for the different electrodes.
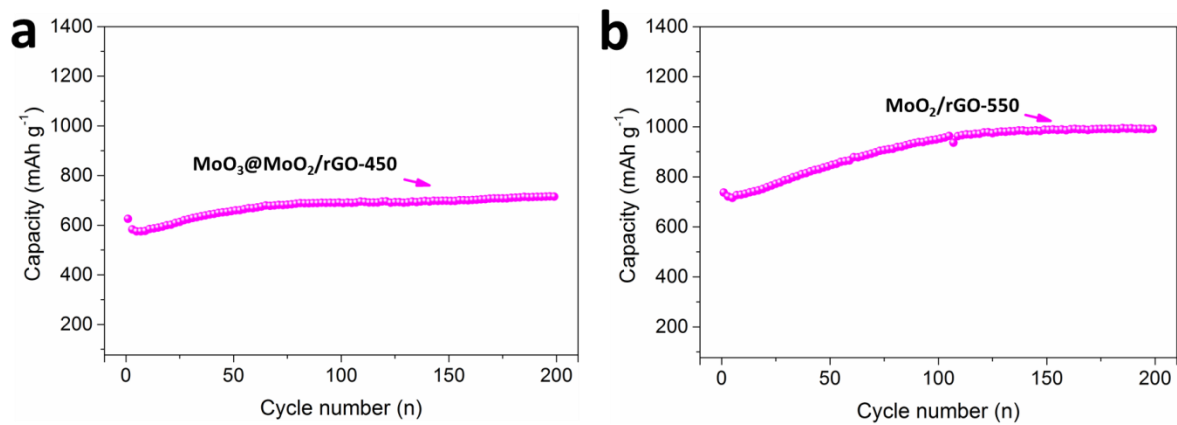
13

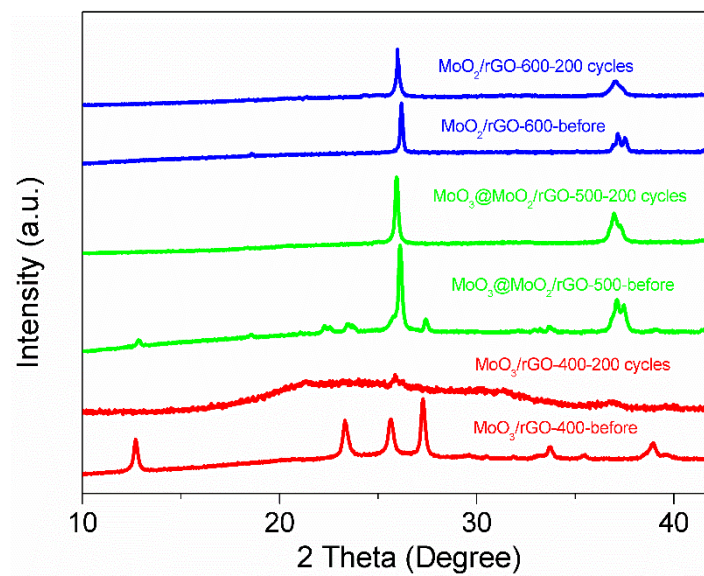**Figure S12.** Cycling performance for 200 cycles at 2 A g^{-1}: (a) MoO$_3$@MoO$_2$/rGO-450, (b) MoO$_2$/rGO-550 electrodes.

Figure S13. XRD pattern changes of MoO$_3$/rGO-400, MoO$_3$@MoO$_2$/rGO-500, and MoO$_2$/rGO-600 electrodes before cycling and after 200 cycles.
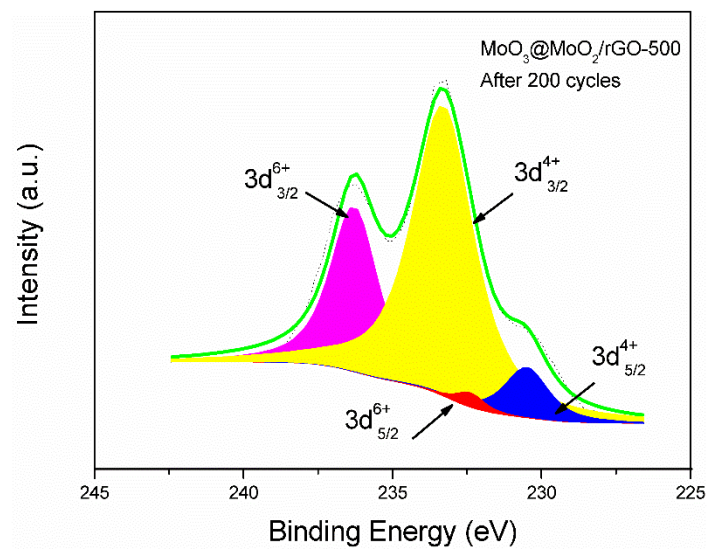
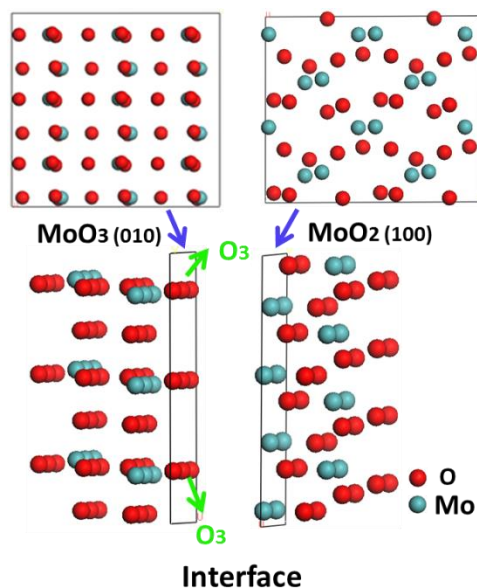**Figure S14.** Mo 3d XPS spectrum of MoO$_3$@MoO$_2$/rGO-500 electrode after 200 cycles.

Figure S15. The models for the $MoO_3(010)$ and $MoO_2(100)$ slabs. According to the solid-state reaction kinetics of the reduction of α-MoO_3, the lattice oxygen $O_{(3)}$ along the (010) facet is reduced as the temperature increases, resulting in oxygen vacancies.[4] The formation of oxygen vacancies at the $O_{(1)}$ and $O_{(2)}$ sites is significantly less favourable than at the $O_{(3)}$ site. This is because the vacancy structure at the $O_{(3)}$ site, where two polarons occupy the d_{xy} and d_{yz} orbitals of the five-fold coordinated Mo^{4+} ion at the defect, is 0.19 eV higher in energy.[5, 6] The re-organization of lattice oxygen takes place in the MoO_3 bulk along the [100] or [001] direction, forming defects in the structure, and the lattice oxygen at the surface of the (010) facet is replenished. This is because oxygen diffusion along the [100] or [001] directions in the MoO_3 layered structure is much faster than parallel to the layers ([010] direction). After a certain concentration of oxygen vacancies in the MoO_3 structure has been exceeded, the oxygen vacancies are consumed by forming intermediate phase Mo_4O_{11} ($3MoO_3 \cdot MoO_2$) impurities, which serve as nucleation sites for the rapid formation of MoO_2 crystallites. The mechanism for the formation of MoO_2 structure seems to be strongly dependent on the layered structure in the [010] direction of MoO_3, seeing that the various

orientations of MoO_2 crystallites correspond to some boundary planes in MoO_2, which have a structure very close to the (010) planes in the semi-layer.[7] The reduction brings about the collapse of the successive (010) planes of MoO_3. In this transformation, the <100> rows in MoO_2, constituted by strongly linked elements (edge-sharing MoO_6 octahedra) are found to be arranged in some directions perpendicular or very oblique with respect to the initial (010) surface of MoO_3. Specifically, the (010) lattice plane of MoO_3 is converted into the (100) facet of MoO_2 as the temperature increases. The lattice plane size details: MoO_3 (010): $a = 11.0892$ Å, $b = 11.8884$ Å; MoO_2 (100): $a = 9.7132$ Å, $b = 11.0892$ Å.
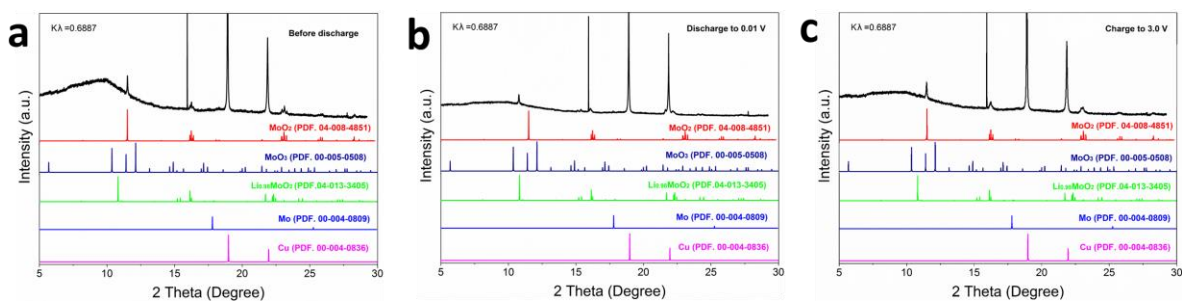
Figure S16. In-operando synchrotron XRPD data for $MoO_3@MoO_2/rGO-500$ electrode: (a) before discharge, (b) after discharge to 0.01 V, and (c) after charge to 3.0 V. Before discharge, the XRPD pattern matches well with MoO_2 (K λ = 0.6887 Å). The main peaks of the XRPD pattern match ideally with $Li_{0.98}MoO_2$ on discharging to 0.01 V. In the meantime, a small peak located at about 17.9° can be observed, which means that the $MoO_3@MoO_2$ heterostructures have been partially converted into Mo. When the cell is charged to 3.0 V, the XRPD pattern shows similar peaks to the original pattern, indicating the good phase reversibility of MoO_2, which helps to relieve the pulverization of α-MoO_3.
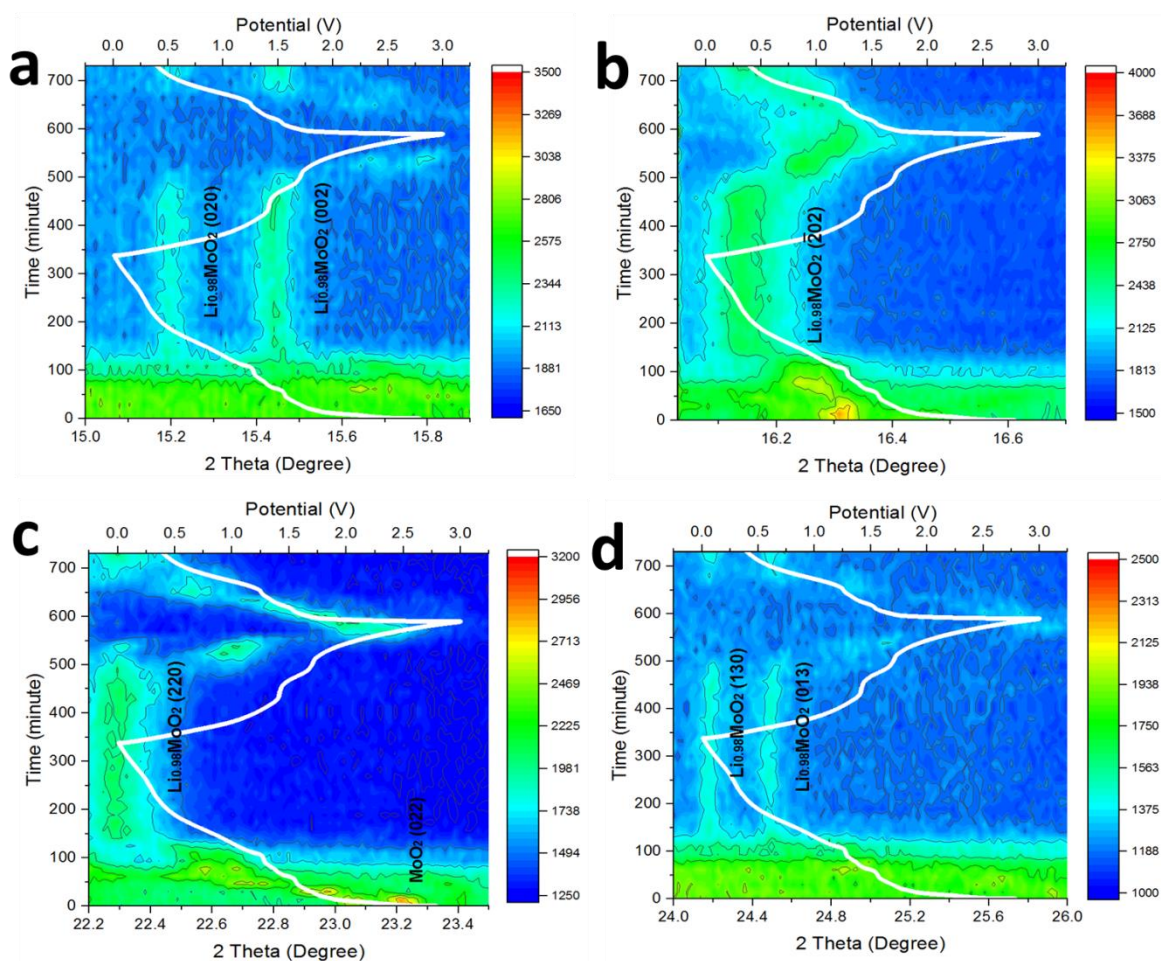
Figure S17. Contour plots of the in-operando synchrotron XRPD data for MoO$_3$@MoO$_2$/rGO-500 electrode in different degree ranges: (a) 15.0°–15.9°, where the (020) and (002) peaks of Li$_{0.98}$MoO$_2$ appear in the discharge process; (b) 16.0°–16.8°, where the ($\bar{2}$02) peak of Li$_{0.98}$MoO$_2$ appears; (c) 22.2°–23.6°, where the (022) peak of MoO$_2$ is converted to the (220) peak of Li$_{0.98}$MoO$_2$; and (d) 24.0°–26.0°. (Note that the synchrotron coin cell was perpendicularly placed on the sample stage, so that the excess electrolyte flowed to the bottom of the cell due to gravity, resulting in a significant drop of the background signal)

References

1.   Gao, H.; Zhou, T.; Zheng, Y.; Zhang, Q.; Liu, Y.; Chen, J.; Liu, H.; Guo, Z., Cos Quantum Dot Nanoclusters for High-Energy Potassium-Ion Batteries. Adv. Funct. Mater. **2017,** *27*, 1702634.

2.   Mai, L. Q.; Hu, B.; Chen, W.; Qi, Y.; Lao, C.; Yang, R.; Dai, Y.; Wang, Z. L., Lithiated MoO_3 Nanobelts with Greatly Improved Performance for Lithium Batteries. Adv. Mater. **2007,** *19*, 3712-3716.

3.   Dahn, J. R.; McKinnon, W. R., Structure and Electrochemistry of Li_xMoO_2. Solid State Ionics **1987,** *23*, 1-7.

4.   Lalik, E., Kinetic Analysis of Reduction of MoO_3 to MoO_2. Catal. Today **2011,** *169*, 85-92.

5.   Bhaskar, A.; Deepa, M.; Rao, T. N.; Varadaraju, U. V., Enhanced Nanoscale Conduction Capability of a MoO_2/Graphene Composite for High Performance Anodes in Lithium Ion Batteries. J. Power Sources **2012,** *216*, 169-178.

6.   Dieterle, M.; Weinberg, G.; Mestl, G., Raman Spectroscopy of Molybdenum Oxides - Part I. Structural Characterization of Oxygen Defects in MoO_{3-X} by DR UV/Vis, Raman Spectroscopy and X-Ray Diffraction. Phys. Chem. Chem. Phys. **2002,** *4*, 812-821.

7.   Scanlon, D. O.; Watson, G. W.; Payne, D. J.; Atkinson, G. R.; Egdell, R. G.; Law, D. S. L., Theoretical and Experimental Study of the Electronic Structures of MoO_3 and MoO_2. J. Phys. Chem. C. **2010,** *114*, 4636-4645.